

High-Density and Freestanding Porous Carbon Film for Compact Sodium-Ion Storage

Xiaomin Lin,^[a] Weicai Zhang,^{*[a, b]} Jiaao Chen,^[a] Jiacong Lu,^[a] Mingtao Zheng,^[a, c] Yingliang Liu,^[a, c] and Yeru Liang^{*[a, c]}

Porous carbon materials are often difficult to achieve high density while possessing high porosity, which limits their application in compact energy storage. Here, a design of freestanding porous-yet-dense carbon films with a tunable density ($1.08\text{--}1.33\text{ g cm}^{-3}$) and porosity (specific surface area of $0\text{--}423.8\text{ m}^2\text{ g}^{-1}$) is presented through an assembly of porous carbon nanosheet with graphene oxide under vacuum filtration. The typical freestanding carbon films simultaneously deliver a high density of 1.08 g cm^{-3} and a high specific surface area of

$423.8\text{ m}^2\text{ g}^{-1}$ when the porous carbon nanosheet content is 75 wt.%. As anode materials for sodium-ion batteries, the optimized freestanding carbon films deliver high volumetric capacity (270 mAh cm^{-3} at 20 mA g^{-1}), high initial capacity efficiency (81%) and superior long-term cycling stability (1300 cycles with a capacity decay rate of 0.012% per cycle). This study provides a promising direction for creating freestanding electrodes that meet both high-porosity and high-density requirements for compact sodium-ion batteries.

Introduction

By incorporating the advantages of carbon materials with porous solid, porous carbon has gained increasing attention from both academic and industrial communities.^[1] High porosity has been always pursued for the development of porous carbons.^[2] Main motivation behind this activity is high porosity provides large area for dispersion of active sites and then open unprecedented opportunities for advances in the emerging application performance or further extension in their application ambit.^[3] Nonetheless, the introduction of high porosity into carbon materials usually leads to a low density (generally $0.1\text{--}0.6\text{ g cm}^{-3}$) due to the huge amount of void.^[4] This will reduce their volumetric capability and hinders the practical use in compact applications.^[5] In addition, porous carbons are typically performed in powder forms that always cause some defects in the actual application.^[6] For example, those porous carbon powders cannot perform well under different types of mechanical stresses and exhibits poor recyclability, which streamline the practical application process.^[7]

To address these drawbacks, significant efforts have been made to densify porous carbons into freestanding forms by developing various strategies.^[8] One of the most effective approaches is compressing porous carbon particles by utilizing polymer binder.^[9] This strategy enables the concurrent formation of self-supported porous carbon with high density. However, a high pressures ($>100\text{ MPa}$) easily destroys the inherent structure of porous carbon and result in limited density improvement ($\sim 0.7\text{ g cm}^{-3}$), as it only reduces interparticle voids.^[10] Moreover, the accessible surface area would be reduced by the inactive binder, which leads to sluggish molecular/ion transport and deteriorates the actual performances.^[11] Therefore, achievement of both high density and high porosity still poses a significant challenge for porous carbon.

In recent years, graphene-based materials are proposed as building blocks to synthesize porous-yet-dense carbonaceous freestanding forms due to their two-dimensional sheet-like structure for easy dense stacking, excellent mechanical robustness, electrical conductivity and flexibility.^[12] For example, Tang *et al.* reported a compact graphene framework with a density of 1.2 g cm^{-3} through converting traditional graphene oxide (GO) into nano-sized GO.^[13] Liu *et al.* developed an efficient strategy to prepare self-assembly reduced GO (rGO) with high packing density (1.55 g cm^{-3}) through phosphoric acid treatment approach at high temperature.^[14] Despite of these impressive advances, the as-obtained densified graphene-based materials normally encounter low specific surface area (in most case, $10\text{--}200\text{ m}^2\text{ g}^{-1}$), mainly due to the nonporous or poor porous carbonaceous framework.^[15] This will reduce the amount of available surface area and/or ion diffusion channels, which lead to insufficient sites for energy storage and low ion accessibility to the active sites.^[16] High porosity and density, in general, are mutually exclusive and hard to attain simultaneously.^[17] The balance of porosity and density of porous carbons remains a formidable challenge.

[a] X. Lin, Dr. W. Zhang, J. Chen, J. Lu, Prof. M. Zheng, Prof. Y. Liu, Prof. Y. Liang
Key Laboratory for Biobased Materials and Energy of Ministry of Education, Guangdong Provincial Engineering Technology Research Center for Optical Agriculture
College of Materials and Energy, South China Agricultural University
510642 Guangzhou, P. R. China
E-mail: liangyr@scau.edu.cn

[b] Dr. W. Zhang
Songshan Lake Materials Laboratory (SLAB)
523808 Dongguan, P. R. China
E-mail: zhangweicai@sslab.org.cn

[c] Prof. M. Zheng, Prof. Y. Liu, Prof. Y. Liang
Maoming Branch, Guangdong Laboratory of Lingnan Modern Agriculture
525000 Maoming, P. R. China

 Supporting information for this article is available on the WWW under <https://doi.org/10.1002/batt.202400117>

In this work, we presented freestanding porous-yet-dense carbon films with tunable density ($1.08\text{--}1.33\text{ g cm}^{-3}$) and specific surface area (SSA) ($0\text{--}423.8\text{ m}^2\text{ g}^{-1}$) by using an assembly strategy. The freestanding films can be simply fabricated by rational assembly of GO with porous carbon nanosheet (PCS) through directional vacuum filtration, which were subjected to a near-parallel arrangement (Figure 1). The balance of the porosity and density is achieved by tuning the PCS content, which exhibits a high density of 1.08 g cm^{-3} and high SSA of $423.8\text{ m}^2\text{ g}^{-1}$ simultaneously when the PCS content accounts for 75%. The as-prepared porous-yet-dense carbonaceous films can be used as freestanding anodes for sodium ion batteries without binders, conductive agents and current collectors. The sodium storage mechanism of the freestanding anodes was studied by galvanostatic intermittent titration (GITT) and ex situ X-ray diffraction (XRD). It was revealed that sodium ions adsorb in surface sites, insert into the edge of graphitic-like domains at high voltage and fill in micropores at low voltage. Benefiting from the abundant ultramicroporous and well-organized composite structure, the typical freestanding porous-yet-dense carbon film anode exhibited impressive electrochemical performances with a high initial capacity efficiency (ICE) of 81%, high volumetric capacity (270 mAh cm^{-3} at 20 mA g^{-1}) and superior long-term cycling stability (1300 cycles with a capacity decay rate of 0.012% per cycle).

Results and Discussion

Fabrication of High-Density and Freestanding Porous Carbon Film

The fabrication of freestanding porous-yet-dense carbon films (*i.e.*, PCS-rGO-x, where x represents the percentage of PCS content) as schematically illustrated in Figure 2a. First, we employed a surface-limited assembly method combined with vacuum filtration to synthesize PCS by using tannic acid as precursor, Pluronic F127 as soft template and NaCl as salt substrate.^[18] The morphology of PCS was characterized by scanning electron microscopy (SEM) and transmission electron microscopy (TEM), which show PCS possesses two-dimensional porous structure (Figure S1). The Fourier transform infrared spectroscopy of PCS showed the presence of hydroxyl (3423 cm^{-1}), carbonyl (1606 cm^{-1}) and epoxy (1284 cm^{-1}) groups, which contributed to its good hydrophilic property (Figure S2). Next, the homogeneous precursor suspension combined with PCS and GO was performed by means of ultrasonic treatment for 30 minutes (Figure S3). The film structure was created from the homogeneous suspension of PCS and GO by vacuum filtration. The vacuum-assisted assembly and electrostatic repulsion interaction between the PCS and GO sheets facilitated stacking of the PCS and GO in a laminated fashion, yielding a flexible and freestanding composite film (PCS-GO-x film) (Figure S4–S6). The porosity and density of PCS-GO-x films can be precisely regulated by means of adjusting content of PCS (Figure 2b–e).

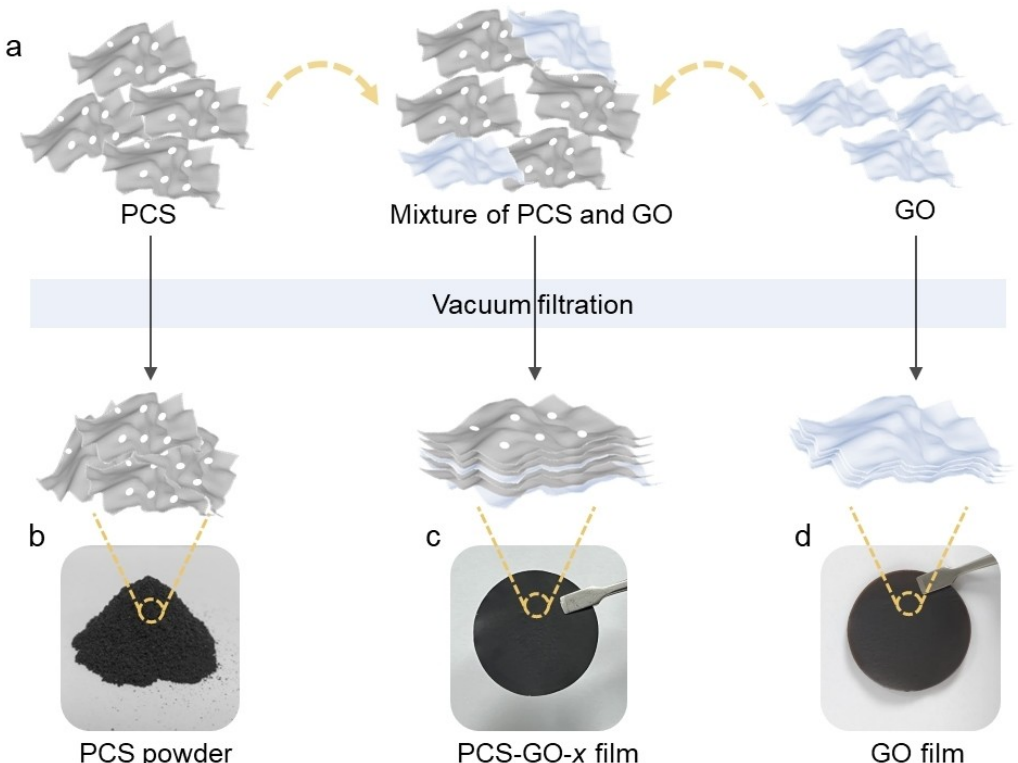


Figure 1. (a) Schematic diagram illustrating the synthesis of freestanding PCS-GO-x film. Digital photos of (b) PCS powder, (c) PCS-GO-x film and (d) GO film.

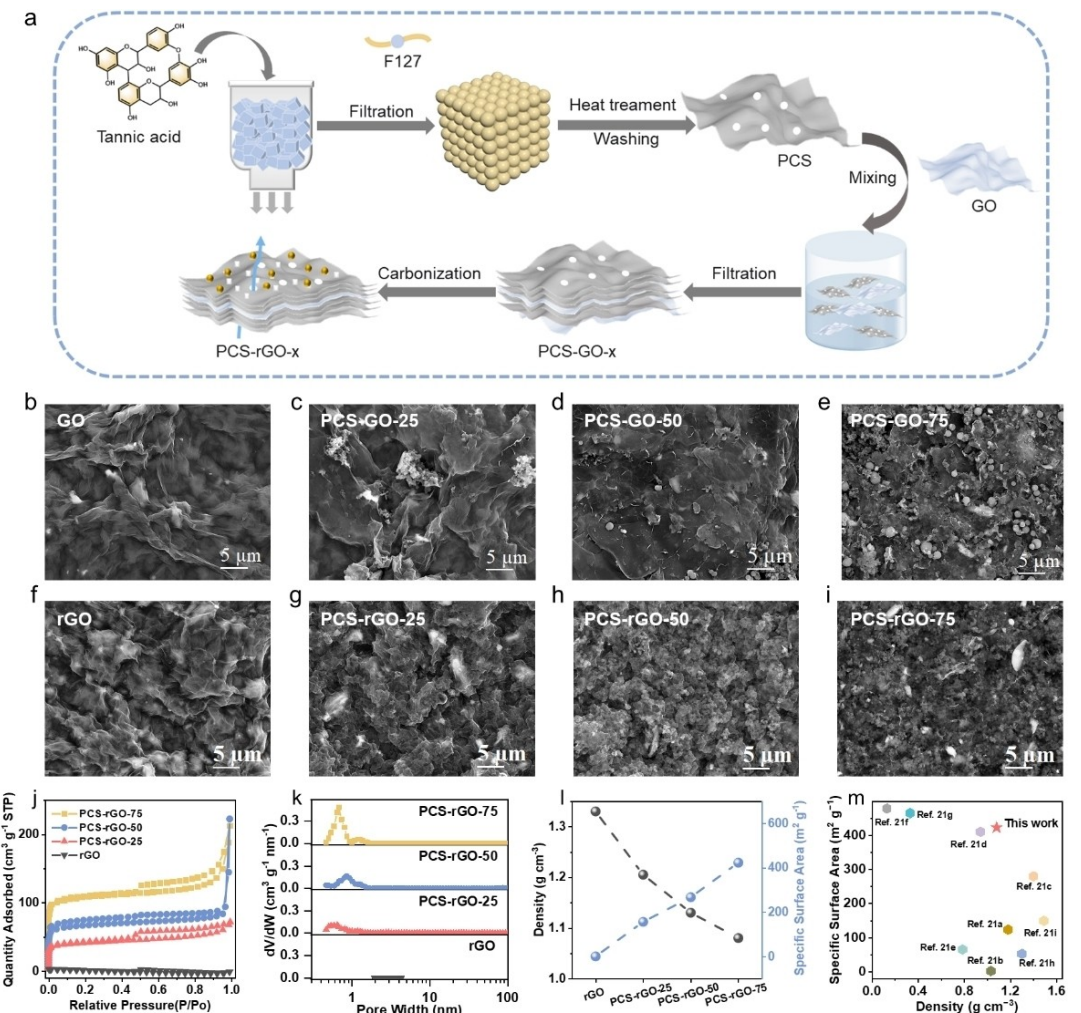


Figure 2. (a) Schematic illustration of the synthesis process of PCS-rGO-x films. SEM images of (b–e) PCS-GO-x and (f–i) PCS-rGO-x films. (j) Nitrogen adsorption–desorption isotherms, (k) pore-size distributions, and (l) the relationship of SSA and density of PCS-rGO-x films. (m) Comparison of density and SSA of PCS-rGO-75 film with other graphene-based carbonaceous materials.

After a high-temperature treatment of 600 °C under N₂ flow, the GO in PCS-GO-x films undergoes a reduction reaction to yield rGO, obtaining the PCS-rGO-x films. The XRD patterns of PCS-rGO-x films display two typical broad diffraction peaks at 2θ of ≈23° and ≈42° of amorphous carbon (Figure S7), revealing their nongraphite structures.^[19] SEM image in Figure 2f shows that rGO has a tightly stacked two-dimensional sheet-like structure, which is conducive to the formation of high-density freestanding films. As the PCS content increases, the surface morphologies of PCS-GO-x films tend to transition from two-dimensional sheet-like to dense and porous three-dimensional network structure (Figure 2g–i), indicating the formation of more ion transport channels and ion storage active sites. Cross-sectional SEM images of PCS-rGO-x films show a parallel stacked structure, which is key to achieve high flexibility and high mechanical strength (Figure S8). N₂ adsorption/desorption measurements show PCS-rGO-x films possess higher SSA and porosity when the content of the PCS is increased (Figure 2j), which confirms that the pore structure of PCS-rGO-x films can be controlled by varying the PCS content. Note that the

addition of PCS can greatly increase the microporous content of PCS-rGO-x films, with the microporous area increasing from 0 to 375.7 m² g⁻¹ and the microporous volume increasing from 0 to 0.14 cm³ g⁻¹ (Table S1). The pore size distribution curves indicate that the size of micropores is largely concentrated at 0.59–0.85 nm in the PCS-rGO-x films (Figure 2k and Figure S9), with a large number of ultramicropores with size below 0.7 nm, which are considered necessary for gaining high-rate capacity and high ICE in sodium-ion batteries.^[20] The PCS-rGO-x films are not only rich in micropores but also maintain a considerable density (1.08–1.33 g cm⁻³), which favors volumetric performance. In addition, the density of the PCS-rGO-x films is tunable by changing the PCS content, whereas SSA shows the opposite trend (Figure 2l). Among them, the as-constructed PCS-rGO-75 film can achieve SSA of 423.8 m² g⁻¹ and still maintain a high density of 1.08 g cm⁻³. Therefore, compared with the previously reported graphene-based materials, the freestanding PCS-rGO-75 film demonstrates the advantage of densely packed structure with balanced porosity and density compared with

previously reported graphene-based carbon (Figure 2m and Table S2).^[21]

Sodium-Ion Storage Performance and Mechanism

To explore the practical application of the synthesized films, the sodium-ion (Na-ion) storage properties of PCS-rGO-x films were examined as freestanding anodes in 2032 coin-type half-cells (Figure 3a). The rate performances of all anodes are measured from 20 to 1000 mAh g⁻¹ as presented in Figure 3b. There is a clear tendency of enhanced gravimetric capacities of the PCS-rGO-x anodes with the elevation in the proportion of PCS. Specifically, the PCS-rGO-75 anode exhibited the highest

gravimetric capacities among all anodes, with values of 250, 216, 195, 177, 162 and 145 mAh g⁻¹ at 20, 50, 100, 200, 500, and 1000 mAh g⁻¹, respectively, which are significantly higher than those of rGO film anode. Figure 3c displays the volumetric capacities of the PCS-rGO-x anodes at different current densities. Among them, the PCS-rGO-75 can deliver high reversible volumetric capacities of 270, 234, 211, 192, 175, 157 mAh cm⁻³ at 20, 50, 100, 200, 500 and 1000 mAh g⁻¹, respectively. While the volumetric capacities of rGO anode are only 183, 174, 165, 154, 138 and 122 mAh cm⁻³, respectively. The as-fabricated high-density freestanding anode also possesses better volumetric capacity compared with other reported hard carbon-based anodes (Figure S10 and Table S3), showing its superiority in compact Na-ion storage.^[21e,f,h,22]

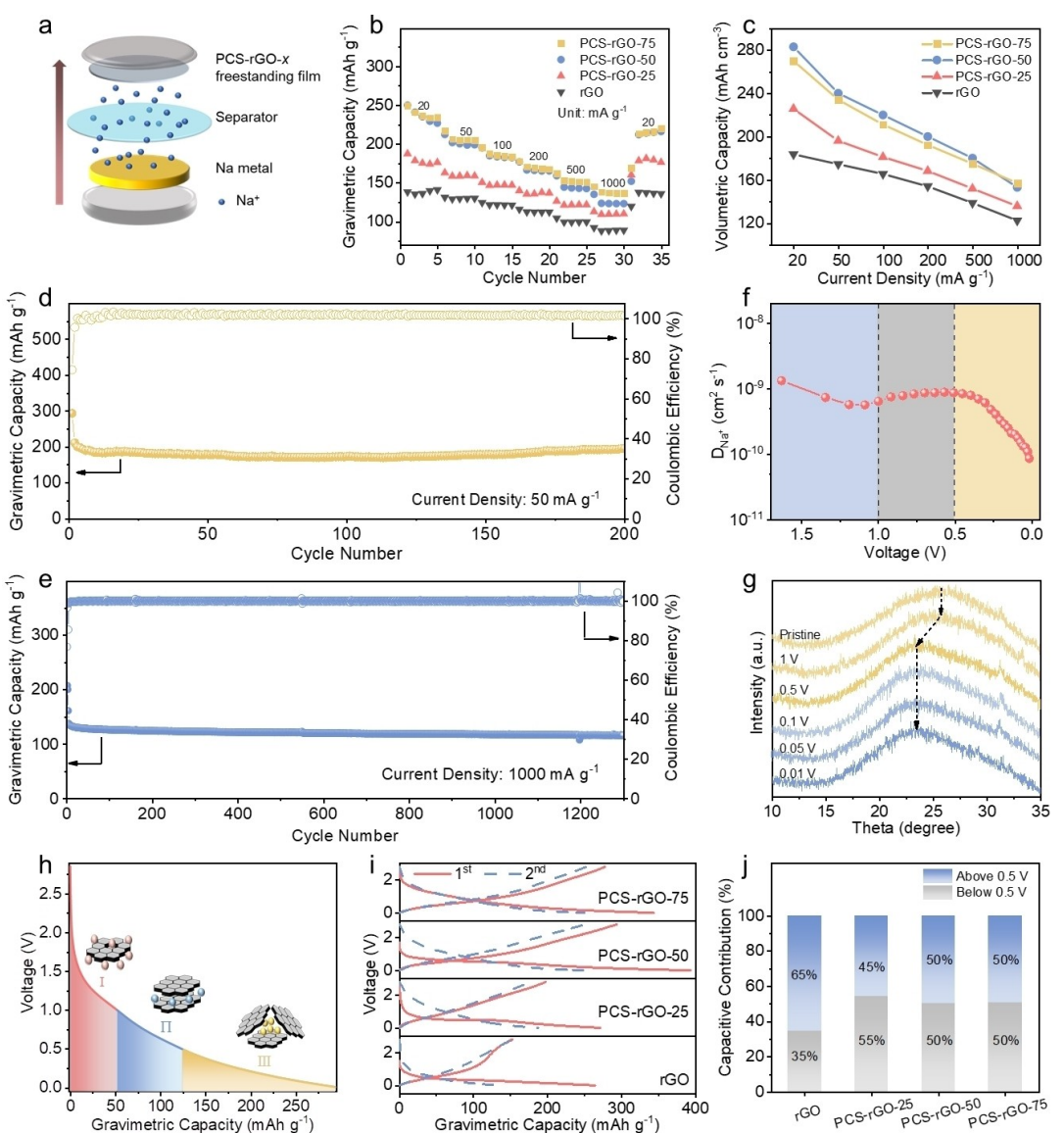


Figure 3. (a) Schematic illustration of coin-type half-cell using PCS-rGO-x as anodes. (b) Rate performances of PCS-rGO-x from 20 to 1000 mAh g⁻¹. (c) Volumetric capacitances versus current densities of PCS-rGO-x. Cycling performances of PCS-rGO-75 under (d) 50 mA g⁻¹ and (e) 1000 mA g⁻¹, in which the current density of initial three cycles was 50 mA g⁻¹. (f) Na⁺ diffusion coefficients of PCS-rGO-75 calculated from GITT potential profiles for the discharge process. (g) The ex-situ XRD patterns during the sodiation process and (h) illustration of the sodium storage mechanism of PCS-rGO-75. (i) The first galvanostatic discharge/charge profiles of PCS-rGO-x at 20 mA g⁻¹. (j) The contribution ratios of capacities of PCS-rGO-x above 0.5 V (blue) and below 0.5 V (gray) at 20 mA g⁻¹.

To further explore the long cycling performance, PCS-rGO-75 anode is measured at a current density of 50 mA g^{-1} , presenting a reversible discharge capacity of 212 mAh g^{-1} with ICE of 75% and retention capacity of 196 mAh g^{-1} after 200 cycles, corresponding to a capacity retention of 93% (Figure 3d and Figure S11). In addition, at the same current density, rGO, PCS-rGO-25 and PCS-rGO-50 just display a reversible capacity of 114, 160 and 186 mAh g^{-1} with ICE of 53%, 58% and 68%, and provide a capacity of 129, 159 and 174 mAh g^{-1} after 100 cycles, respectively (Figure S12). Furthermore, when measured at 1000 mA g^{-1} , PCS-rGO-75 anode still delivers a reversible capacity of 137 mAh g^{-1} and maintains a stable discharge capacity of 116 mAh g^{-1} after 1300 cycles, with a capacity decay rate of 0.012% per cycle (Figure 3e).

To study the underlying reasons for the remarkable performance of PCS-rGO-75 anode, we investigated its sodiation mechanism through the evaluation of kinetics by using GITT measurements (Figure 3f and S13). It was found that diffusivity for the sodiation process descends slightly with voltage drop to 1 V and followed appears approximately the same with voltage fall to 0.5 V. This is mainly because that the Na ions absorb in the surface sites such as defects, edges and oxygen-containing functional groups during this process.^[23] And after abundant active sites being occupied, the subsequent Na ions will partly insert into the edge of graphitic-like domains.^[24] With further increase in the discharge depth, the value of Na-ion diffusion coefficients (D_{Na^+}) decreases due to the Na-ion bound in micropores.^[25] During the desodiation process, the D_{Na^+} shows a nearly identical trend as the sodiation process, indicating the excellent reversibility of the PCS-rGO-x anode for Na-ion storage.

To further reveal the structural evolution of PCS-rGO-75 electrode, ex-situ XRD was applied to further verify the above sodium storage mechanism by probing the change in the interlayer spacing. Figure 3g shows the ex-situ XRD patterns during the sodiation process from the pristine position to 0.01 V. As the potential decrease, the diffraction peaks gradually shift toward a lower angle, indicating the insertion of Na ions into the graphite lattice with an expansion of interlayer spacing. However, with the further decrease of voltage, there is no noticeable shift of the diffraction peaks (002), suggesting that there is no obvious intercalation occurring. According to the above results, it can be observed that the discharge process can be divided into three stages described below: In stage I, Na ions first absorb in surface sites including edges, defects, and some of the oxygen-containing functional groups ($> 1.0 \text{ V}$). In stage II, the Na ions favor intercalation into the edge of graphitic-like domains (1.0–0.5 V). In stage III, the Na ions fill in the micropores (0.5–0.01 V).^[26] The relevant explanation model of Na ion storage mechanism is shown in Figure 3h.

To further confirm the accuracy of the above sodium storage mechanism, the discharge-charge profiles of the galvanostatic discharge-charge curves were observed at 20 mA g^{-1} , which display the initial reversible capacities of rGO, PCS-rGO-25, PCS-rGO-50 and PCS-rGO-75 anodes are 152, 197, 293 and 277 mAh g^{-1} , corresponding to ICE of 57, 72, 74 and 81%, respectively (Figure 3i). As the PCS concentration in-

creases, the PCS-rGO-x anodes show higher reversible capacities and ICES. This can be attributed to PCS having abundant ultramicropores, which can offer transport channels for Na-ion insertion and retard the solid electrolyte interphase (SEI) film formation by hindering the contact between the carbon surface and the electrolyte.^[20,27] It is precisely due to the effect of the ultramicropores structure that the deinsertion capacities of PCS-rGO-x anodes below 0.5 V versus Na/Na⁺ achieve or exceed 50% of the whole reversible capacities, which exceeding the 35% of rGO (Figure 3j). To reveal the difference of sodium storage mechanism between PCS and GO, the GITT and ex-XRD of rGO anode were also tested. The GITT curve shows that the diffusivity for the sodiation process descends with voltage drop to about 1.0 V, then rise slightly to 0.5 V and followed descends with voltage fall to 0.01 V. Additionally, the ex-XRD patterns show that the diffraction peaks keep the same as the voltage from pristine to 0.5 V, and shift to a lower angle until discharge process is complete (Figure S14). Combined with the results of GITT and ex-XRD, we infer that sodium ions firstly absorb in surface sites of rGO (edges, defects and oxygen-containing functional groups), and then intercalated between rGO layers, which is different from PCS-rGO-75.^[28]

Kinetic Characterization

The investigation of Na-ions diffusion properties was conducted through electrochemical impedance spectroscopy (EIS). At the fresh states, the Nyquist plots of the PCS-rGO-x anodes are shown in Figure 4a, where the semicircle at high and medium frequency is related to the ohmic resistance (R_s) and charge transfer resistance (R_{ct}), and the oblique line corresponds to the Warburg resistance of Na ions in the bulk carbon.^[29] The calculated R_{ct} of rGO, PCS-rGO-25, PCS-rGO-50, and PCS-rGO-75 are 1000, 750, 500, and 250Ω , respectively. Figure 4b illustrates a linear relationship between the Z'' and the square root of the frequency ($\omega^{-1/2}$) in the low frequency Warburg region of Figure 4a. Moreover, the D_{Na^+} of all four samples were calculated using the Warburg diffusion in the low-frequency linear region of EIS.^[30] The D_{Na^+} of rGO, PCS-rGO-25, PCS-rGO-50, and PCS-rGO-75 were 8.42×10^{-15} , 1.41×10^{-14} , 1.44×10^{-13} , and $1.3 \times 10^{-12} \text{ cm}^2 \text{s}^{-1}$, respectively (Figure 4c). These results suggest that PCS-rGO-x anodes exhibit a faster Na-ion diffusion rate compared to rGO anode, leading to improved rate performance. The increased diffusion kinetics of PCS-rGO-x is mainly attributed to the internal reaction sites within the layer-by-layer stacked framework, which increase the Na-ion affinity, inducing the adsorption of Na ions from the surface to the interior, and maximizing the use of active sites.^[31]

To further investigate the kinetics of ion transportation, the PCS-rGO-75 was assessed using cyclic voltammetry (CV) techniques at various sweep rates ranging from 0.1 to 2.0 mV s^{-1} . Figure 4d illustrates the CV curves for PCS-rGO-75 over a voltage range of 0.01–2.80 V at different sweep rates. With the increase in the scan rate, the CV curves demonstrate analogous peak positions, marginally migrating towards higher potentials. This transformation is likely linked to different types

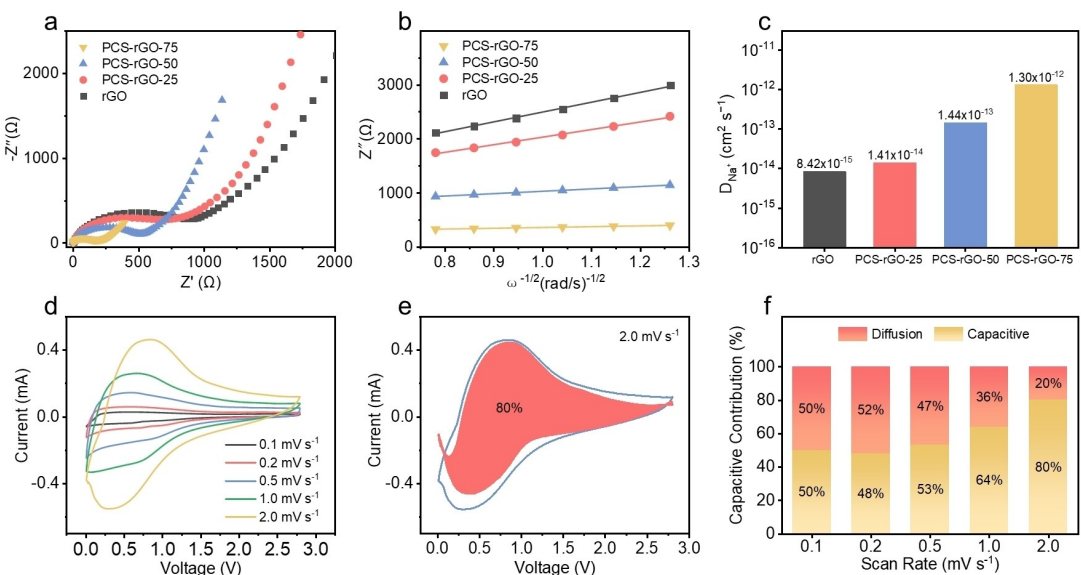


Figure 4. (a) Nyquist plots, (b) the relationship between Z''/Z and $\omega^{-1/2}$ and (c) D_{Na^+} of PCS-rGO-x and rGO electrodes. (d) CV curves at different scan rates, (e) CV curve with the capacitive contribution at a scan rate of 2.0 mV s^{-1} and (f) the capacitive contributions from capacitive (yellow) and diffusion (red) controlled processes measured at various scan rates of PCS-rGO-75.

of capacity storage mechanisms, encompassing pseudo-capacitive contribution and diffusion contribution, with the former progressively assuming a predominant role as the scan rate escalates.^[32] Furthermore, the capacitive contribution can be quantified by applying the equations:^[33]

$$i(v) = k_1 v + k_2 v^{1/2} \quad (1)$$

The $k_1 v$ and $k_2 v^{1/2}$ terms represent the diffusion and capacitive behavior contributions from the total capacity, respectively. The voltage-current profile indicates that the capacitive contributions is around 50% at a sweep rate of 0.1 mV s^{-1} , and increases to approximately 80% when the sweep rate is raised to 2.0 mV s^{-1} (Figure 4e). This trend is depicted in Figure 4f, which displays the variations in capacity contribution ratios at different sweep rates (ranging from 0.1 to 2.0 mV s^{-1}). These findings imply that a great number of the reversible capacity of PCS-rGO-75 anode for Na-ion storage originates from the rapid capacitive action.^[34] It is worth noting that the full use of the capacitive slope region may also enhance battery security by mitigating Na plating and polarization.^[35]

Conclusions

In summary, we have demonstrated an efficient method to produce freestanding porous-yet-dense carbon films. The PCS-rGO-x films are composed of PCS and GO, which is capable to stack in a laminated fashion through vacuum suction filtration. Through tuning the mass ratio of PCS to GO, the density and the SSA of the PCS-rGO-x were regulated from 1.08 g cm^{-3} and from 0 to $423.8 \text{ m}^2 \text{ g}^{-1}$ respectively. With the introduction of PCS, PCS-rGO-x films possessed abundant ultra-

microporous structure with abundant active sites. The obtained PCS-rGO-x could be used as freestanding anodes of sodium ion battery, which delivered high volumetric capacities, high ICES, good rate capability, and impressive cycle stability. The PCS-rGO-x films hold a promising application prospective as free-standing electrode materials of flexible and robust batteries.

Supporting Information

The authors have cited additional references within the Supporting Information.

Acknowledgements

The authors gratefully acknowledge financial support from the projects of the Independent Research Project of Maoming Laboratory (2022ZD002), National Natural Science Foundation of China (52373074), China Postdoctoral Science Foundation (2023M742520) and Guangdong Basic and Applied Basic Research Foundation (2024B1515020017, 2023A1515110190).

Conflict of Interests

The authors declare no conflict of interest.

Data Availability Statement

The data that support the findings of this study are available from the corresponding author upon reasonable request.

Keywords: Porous carbon film • Freestanding • High density • Compact storage • Sodium ion battery

- [1] a) V. Valtchev, L. Tosheva, *Chem. Rev.* **2013**, *113*, 6734; b) M. E. Davis, *Nature* **2002**, *417*, 813; c) P. F. Yu, W. C. Zhang, Y. L. Liu, M. T. Zheng, F. Xu, Y. R. Liang, *Carbon* **2021**, *182*, 100; d) Q. Li, Z. Cao, H. Cheng, J. Zhang, Z. Ma, W. Wahyudi, L. Cavallo, Q. Sun, J. Ming, *ACS Materials Lett.* **2022**, *4*, 2469.
- [2] a) B. W. Li, H. Xiong, Y. Xiao, *Int. J. Electrochem. Sci.* **2020**, *15*, 1363; b) Z. P. Li, P. F. Yu, W. H. Zhong, M. L. Zhang, Z. H. Li, A. Chen, Y. R. Lian, L. Miao, X. Q. Yang, H. Y. Zhan, *Carbon* **2021**, *176*, 1.
- [3] a) B. Szczesniak, J. Phuriragpitikhon, J. Choma, M. Jaroniec, *J. Mater. Chem. A* **2020**, *8*, 18464; b) Y. R. Liang, C. Yang, H. W. Dong, W. Q. Li, H. Hu, Y. Xiao, M. T. Zheng, Y. L. Liu, *ACS Sustainable Chem. Eng.* **2017**, *5*, 7111.
- [4] J. W. Han, H. Li, D. B. Kong, C. Zhang, Y. Tao, H. Li, Q. H. Yang, L. Q. Chen, *ACS Energy Lett.* **2020**, *5*, 1986.
- [5] Y. Tao, X. Xie, W. Lv, D. M. Tang, D. Kong, Z. Huang, H. Nishihara, T. Ishii, B. Li, D. Goldberg, F. Kang, T. Kyotani, Q. H. Yang, *Sci. Rep.* **2013**, *3*, 2975.
- [6] L. L. Gai, K. Li, D. B. Niu, A. L. Zhang, Y. N. Zhang, Y. X. Feng, J. B. Li, T. Liu, *Ind. Crops Prod.* **2023**, *206*, 117701.
- [7] L. Wu, M. Liu, S. Huo, X. Zang, M. Xu, W. Ni, Z. Yang, Y. M. Yan, *Carbon* **2019**, *149*, 627.
- [8] H. Li, Y. Tao, X. Y. Zheng, J. Y. Luo, F. Y. Kang, H. M. Cheng, Q. H. Yang, *Energy Environ. Sci.* **2016**, *9*, 3135.
- [9] F. Ji, L. Wang, J. Yang, X. Wu, M. Li, S. Jiang, S. Lin, Z. Chen, *J. Mater. Chem. A* **2019**, *7*, 1768.
- [10] C. C. Liu, X. J. Yan, F. Hu, G. H. Gao, G. M. Wu, X. W. Yang, *Adv. Mater.* **2018**, *30*, 1705713.
- [11] K. X. Shen, S. L. Zhai, S. F. Wang, Q. Ru, X. H. Hou, K. S. Hui, K. N. Hui, F. M. Chen, *Batteries & Supercaps* **2021**, *4*, 860.
- [12] J. Han, H. Li, Q. H. Yang, *Mater. Today* **2021**, *51*, 552.
- [13] X. Tang, B. Zhou, Q. Ma, Q. Zhang, X. Liu, R. Yang, W. H. Zhang, *J. Power Sources* **2022**, *529*, 231266.
- [14] Z. Liu, L. Wang, G. Ma, Y. Yuan, H. Jia, W. Fei, *J. Mater. Chem. A* **2020**, *8*, 18933.
- [15] a) R. Yuan, Y. Dong, S. Zhang, X. Chen, H. Song, *ACS Appl. Mater. Interfaces* **2021**, *13*, 57092; b) N. Díez, M. Qiao, J. L. Gómez Urbano, C. Botas, D. Carriazo, M. M. Titirici, *J. Mater. Chem. A* **2019**, *7*, 6126; c) J. Zhang, W. Lv, D. Zheng, Q. Liang, D. W. Wang, F. Kang, Q. H. Yang, *Adv. Energy Mater.* **2018**, *8*, 1702395.
- [16] a) C. Tang, M. M. Titirici, Q. Zhang, *J. Energy Chem.* **2017**, *26*, 1077; b) Y. R. Liang, F. X. Liang, D. C. Wu, Z. H. Li, F. Xu, R. W. Fu, *Phys. Chem. Chem. Phys.* **2011**, *13*, 8852.
- [17] Z. N. Li, S. Gadielli, H. C. Li, C. A. Howard, D. J. L. Brett, P. R. Shearing, Z. X. Guo, I. P. Parkin, F. Li, *Nat. Energy* **2020**, *5*, 160.
- [18] L. Liu, X. Yang, Y. Xie, H. Liu, X. Zhou, X. Xiao, Y. Ren, Z. Ma, X. Cheng, Y. Deng, D. Zhao, *Adv. Mater.* **2020**, *32*, 1906653.
- [19] Y. Y. Zhu, M. M. Chen, Q. Li, C. Yuan, C. Y. Wang, *Carbon* **2018**, *129*, 695.
- [20] S. W. Zhang, W. Lv, C. Luo, C. H. You, J. Zhang, Z. Z. Pan, F. Y. Kang, Q. H. Yang, *Energy Storage Mater.* **2016**, *3*, 18.
- [21] a) Y. Yoon, K. Lee, S. Kwon, S. Seo, H. Yoo, S. Kim, Y. Shin, Y. Park, D. Kim, J. Y. Choi, H. Lee, *ACS Nano* **2014**, *8*, 4580; b) J. Yan, Q. Wang, T. Wei, L. L. Jiang, M. L. Zhang, X. Y. Jing, Z. J. Fan, *ACS Nano* **2014**, *8*, 4720; c) Y. Li, D. Zhao, *Chem. Commun.* **2015**, *51*, 5598; d) Q. Wang, J. Yan, Z. J. Fan, *Electrochim. Acta* **2014**, *146*, 548; e) Y. Dong, X. J. Lin, D. K. Wang, R. L. Yuan, S. Zhang, X. H. Chen, L. G. Bulusheva, A. V. Okotrub, H. H. Song, *Energy Storage Mater.* **2020**, *30*, 287; f) M. Yuan, C. Y. Meng, A. Li, B. Cao, Y. Dong, D. K. Wang, X. W. Liu, X. H. Chen, H. H. Song, *Small* **2022**, *18*, 2105738; g) X. J. Lu, H. Dou, S. D. Yang, L. Hao, L. J. Zhang, L. F. Shen, F. Zhang, X. G. Zhang, *Electrochim. Acta* **2011**, *56*, 9224; h) Z. Liu, L. H. Zhang, L. Z. Sheng, Q. H. Zhou, T. Wei, J. Feng, Z. J. Fan, *Adv. Energy Mater.* **2018**, *8*, 1614; i) Y. Xu, Y. Tao, H. Li, C. Zhang, D. H. Liu, C. S. Qi, J. Y. Luo, F. Y. Kang, Q. H. Yang, *Nano Energy* **2017**, *36*, 349.
- [22] a) H. Wang, H. Yuan, W. Zhan, Y. S. Lee, H. J. Shin, X. Wei, Q. Cai, J. L. Lan, Y. Yu, X. Yang, *Carbon* **2020**, *165*, 204; b) A. Beda, F. Rabuel, M. Morcrette, S. Knopf, P. L. Taberna, P. Simon, C. Matei Ghimbeu, *J. Mater. Chem. A* **2021**, *9*, 1743; c) B. Yang, S. Liu, H. Song, J. Zhou, *Carbon* **2019**, *153*, 298.
- [23] a) H. Au, H. Alptekin, A. C. S. Jensen, E. Olsson, C. A. O'Keefe, T. Smith, M. Crespo-Ribadeneyra, T. F. Headen, C. P. Grey, Q. Cai, A. J. Drew, M. M. Titirici, *Energy Environ. Sci.* **2021**, *14*, 3216; b) F. Xie, Z. Xu, A. C. S. Jensen, H. Au, Y. X. Lu, V. Araullo Peters, A. J. Drew, Y. S. Hu, M. M. Titirici, *Adv. Funct. Mater.* **2019**, *29*, 1901072.
- [24] a) H. Yang, R. Xu, Y. Yu, *Energy Storage Mater.* **2019**, *22*, 105; b) C. J. Chen, Y. W. Wen, X. L. Hu, X. L. Ji, M. Y. Yan, L. Q. Mai, P. Hu, B. Shan, Y. H. Huang, *Nat. Commun.* **2015**, *6*, 6929.
- [25] a) Y. Q. Li, Y. X. Lu, Q. S. Meng, A. C. S. Jensen, Q. Q. Zhang, Q. H. Zhang, Y. X. Tong, Y. R. Qi, L. Gu, M. M. Titirici, Y. S. Hu, *Adv. Energy Mater.* **2019**, *9*, 1902852; b) P. X. Bai, Y. W. He, X. X. Zou, X. X. Zhao, P. X. Xiong, Y. H. Xu, *Adv. Energy Mater.* **2018**, *8*, 1703271.
- [26] a) Z. H. Tian, Y. Zhang, J. X. Zhu, Q. Y. Li, T. X. Liu, M. Antonietti, *Adv. Energy Mater.* **2021**, *11*, 2102489; b) Y. Chu, J. Zhang, Y. B. Zhang, Q. Li, Y. R. Jia, X. M. Dong, J. Xiao, Y. Tao, Q. H. Yang, *Adv. Mater.* **2023**, *35*, 2212186; c) Y. Q. Li, A. Vasileiadis, Q. Zhou, Y. X. Lu, Q. S. Meng, Y. Li, P. Ombrini, J. B. Zhao, Z. Chen, Y. S. Niu, X. G. Qi, F. Xie, R. van der Jagt, S. Ganapathy, M. M. Titirici, H. Li, L. Q. Chen, M. Wagemaker, Y. S. Hu, *Nature Energy* **2024**, *9*, 357; d) Z. Tian, Y. Zou, G. Liu, Y. Wang, J. Yin, J. Ming, H. N. Alshareef, *Adv. Sci.* **2022**, *9*, 2201207.
- [27] a) J. L. Xia, D. Yan, L. P. Guo, X. L. Dong, W. C. Li, A. H. Lu, *Adv. Mater.* **2020**, *32*, 2000447; b) Y. Wang, Z. Cao, W. Wahyudi, Z. Ma, Y. Liang, L. Cavallo, Q. Li, J. Ming, *Adv. Energy Mater.* **2023**, *13*, 29.
- [28] J. H. Choe, N. R. Kim, M. E. Lee, H. J. Yoon, M. Y. Song, H. J. Jin, Y. S. Yun, *ChemElectroChem* **2017**, *4*, 716.
- [29] M. X. Song, L. J. Xie, J. Y. Cheng, Z. L. Yi, G. Song, X. Y. Jia, J. P. Chen, Q. G. Guo, C. M. Chen, *J. Energy Chem.* **2022**, *66*, 448.
- [30] Y. Chen, J. Li, Y. Lai, M. Xu, J. Li, P. Wang, Z. Zhang, *ChemSusChem* **2018**, *11*, 1334.
- [31] a) J. Wang, J. Tang, B. Ding, V. Malgras, Z. Chang, X. D. Hao, Y. Wang, H. Dou, X. G. Zhang, Y. Yamauchi, *Nat. Commun.* **2017**, *8*, 15717; b) Y. P. Guo, J. R. Qi, Y. Q. Jiang, S. F. Yang, Z. C. Wang, H. D. Xu, *Mater. Chem. Phys.* **2003**, *80*, 704.
- [32] Y. Chen, J. Li, Y. Lai, M. Yin, Z. Zhang, *J. Energy Chem.* **2018**, *810*, 207.
- [33] B. Jiang, Y. Zhang, D. Yan, J. L. Xia, W. C. Li, *ChemElectroChem* **2019**, *6*, 3043.
- [34] a) G. Wang, M. Shao, H. Ding, Y. Qi, J. Lian, S. Li, J. Qiu, H. Li, F. Huo, *Angew. Chem. Int. Ed.* **2019**, *58*, 13584; b) P. F. Yu, W. C. Zhang, Y. H. Yang, M. T. Zheng, H. Hu, Y. Xiao, Y. L. Liu, Y. R. Liang, *J. Colloid Interface Sci.* **2021**, *582*, 852.
- [35] a) F. Xie, Y. Niu, Q. Zhang, Z. Guo, Z. Hu, Q. Zhou, Z. Xu, Y. Li, R. Yan, Y. Lu, M. M. Titirici, Y. S. Hu, *Angew. Chem. Int. Ed.* **2022**, *61*, e202116394; b) L. Zhou, Z. Cao, J. Zhang, Q. Sun, Y. Wu, W. Wahyudi, J. Y. Hwang, L. Wang, L. Cavallo, Y. K. Sun, H. N. Alshareef, J. Ming, *Nano Lett.* **2020**, *20*, 3247.

Manuscript received: February 23, 2024

Revised manuscript received: April 2, 2024

Accepted manuscript online: April 25, 2024

Version of record online: June 3, 2024